JOURNAL OF Materials CHEMISTRY

Lithium borate–strontium bismuth tantalate glass nanocomposite: a novel material for nonlinear optic and ferroelectric applications

G. Senthil Murugan and K. B. R. Varma*

Materials Research Centre, Indian Institute of Science, Bangalore -560012, India.
E-mail: kbrvarma@mrc.iisc.ernet.in; Fax: 91-80-3600683

Received 27th August 2001, Accepted 14th February 2002
First published as an Advance Article on the web 27th March 2002

Glass nanocomposites in the system $(100 - x)Li_2B_4O_7$–$xSrBi_2Ta_2O_9$ ($0 \leqslant x \leqslant 22.5$, in molar ratio) were fabricated *via* a melt quenching technique followed by controlled heat-treatment. The as-quenched samples were confirmed to be glassy and amorphous by differential thermal analysis (DTA) and X-ray powder diffraction (XRD) techniques, respectively. The phase formation and crystallite size of the heat-treated samples (glass nanocomposites) were monitored by XRD and transmission electron microscopy (TEM). The relative permittivities (ε_r') of the glass nanocomposites for different compositions were found to lie in between that of the parent host glass ($Li_2B_4O_7$) and strontium bismuth tantalate (SBT) ceramic in the frequency range 100 Hz–40 MHz at 300 K, whereas the dielectric loss (D) of the glass nanocomposite was less than that of both the parent phases. Among the various dielectric models employed to predict the effective relative permittivity of the glass nanocomposite, the one obtained using the Maxwell's model was in good agreement with the experimentally observed value. Impedance analysis was employed to rationalize the electrical behavior of the glasses and glass nanocomposites. The pyroelectric response of the glasses and glass nanocomposites was monitored as a function of temperature and the pyroelectric coefficient for glass and glass nanocomposite ($x = 20$) at 300 K were 27 $\mu C\ m^{-2}\ K^{-1}$ and 53 $\mu C\ m^{-2}\ K^{-1}$, respectively. The ferroelectric behavior of these glass nanocomposites was established by P *vs.* E hysteresis loop studies. The remnant polarization (P_r) of the glass nanocomposite increases with increase in SBT content. The coercive field (E_c) and P_r for the glass nanocomposite ($x = 20$) were 727 V cm^{-1} and 0.527 $\mu C\ cm^{-2}$, respectively. The optical transmission properties of these glass nanocomposites were found to be composition dependent. The refractive index ($n = 1.722$), optical polarizability ($\alpha_m = 1.266 \times 10^{23}\ cm^3$) and third-order nonlinear optical susceptibility ($\chi^{(3)} = 3.046 \times 10^{-21}\ cm^3$) of the glass nanocomposite ($x = 15$) were larger than those of the as-quenched glass. Second harmonic generation (SHG) was observed in transparent glass nanocomposites and the d_{eff} for the glass nanocomposite ($x = 20$) was found to be 0.373 pm V^{-1}.

1. Introduction

Bismuth-containing layered compounds belonging to the Aurivillius family with the general formula $[Bi_2O_2]^{2+}$ $[A_{n-1}B_nO_{3n+1}]^{2-}$, where A is in 12-fold coordination, B in 6-fold coordination and n is an integer ranging from 1 to 5, are interesting because of their ferroelectric and other related properties. Thin films of ferroelectric strontium bismuth tantalate ($SrBi_2Ta_2O_9$; SBT) are known to be promising for ferroelectric integrated devices.[1–3] This compound is very attractive particularly for its applications in ferroelectric random access memories (FeRAMs). SBT films are the most promising among the ferroelectric compounds for FeRAMs because they have superior fatigue-free properties and small coercive fields.[1–3] In the last decade, SBT films were well characterized for possible applications in the memory devices. However, the optical properties of this industrially important material were not fully investigated. These properties have recently been recognized to be important from the optical device point of view. There were a few reports available on the optical properties of SBT bulk ceramics[4] and SBT thin films.[5,6] However, there is a need to have optical quality bulk single crystals for specific applications. Unfortunately growing large single crystals of this material is extremely difficult due to its high melting point and dissociation characteristics. Therefore, we have been exploring alternative ways of obtaining transparent materials. One of the routes that attracted our attention has been the glass-ceramic. It would be interesting to visualize the behavior of crystallites of nano/micrometre size embedded in a glass matrix as these crystals are known to give rise to exotic properties. The glass matrix facilitates the engineering of microstructure and physical properties. The expertise that we have in making optical nanocomposites of functional ceramics,[7,8] has been extended to fabricate a glass-ceramic of SBT in a lithium borate glass matrix. Recently, we reported the ferroelectric and non-linear optical properties of this glass-ceramic.[9] Lithium borate ($Li_2B_4O_7$; LBO) was chosen as the glass matrix because of its good glass forming ability and wide optical transmission window.[10] We fabricated this glass-ceramic aiming at the possible applications in electro-optic and non-linear optical devices. To begin with, the electrical properties, which have an indirect influence on the above mentioned properties, were studied. In this paper, we elucidate the details pertaining to the structural, thermal, electrical and optical properties of the $(100 - x)Li_2B_4O_7$–$xSrBi_2Ta_2O_9$ ($0 \leqslant x \leqslant 22.5$) glass nanocomposites.

2. Experimental

Transparent glasses of composition $(100 - x)Li_2B_4O_7$–$xSrBi_2Ta_2O_9$ (x ranging from 0 to 22.5, in molar ratio) were fabricated *via* conventional melt-quenching technique. The required $Li_2B_4O_7$ and $SrBi_2Ta_2O_9$ powders were prepared from their respective oxides (B_2O_3, Bi_2O_3 and Ta_2O_5) and carbonates (Li_2CO_3 and $SrCO_3$) (Aldrich Chemicals) by regular solid state reaction routes. The formation of the crystalline phases of

 DOI: 10.1039/b107794p

$Li_2B_4O_7$ and $SrBi_2Ta_2O_9$ was confirmed by X-ray powder diffraction studies. LBO and SBT in different molar ratios were mixed well using a mortar and pestle in an acetone medium for an hour and transferred to a platinum crucible. The crucible containing the mixture was covered with a lid and placed in a melt-quenching furnace (Lenton), heated to 1375 K (heating rate used was 5 K min^{-1}) and maintained at this temperature for 30 minutes. The crucible containing the molten material was taken out and the melt was poured on to a preheated stainless steel plate and quickly pressed by another stainless steel plate. The flat glass plates thus obtained were annealed at 475 K for 6 h (heating and cooling rate was 50 K h^{-1}) to release thermal stresses that are likely to be associated with them.

The glassy state of the as-quenched samples was established by subjecting them (weighing $\sim$30 mg) to differential thermal analyses (DTA; Polymer Laboratories STA 1500) in the 300 K to 1273 K temperature range. A uniform heating rate of 15 K min^{-1} was employed for this purpose. The average values of the glass transition temperature (T_g) and the temperature of onset of crystallization (T_{cr}) were evaluated based on the DTA data collected on more than four samples.

To ascertain the amorphous and glass nanocomposite nature of the as-quenched and heat treated glasses, X-ray powder diffraction (XRD) (Scintag, USA) studies were carried out using Cu Kα radiation. The XRD patterns obtained for heat-treated samples were compared with those of JCPDS (Joint Committee on Powder Diffraction Standards) data to identify the crystalline phase present in the glass matrix. Structural details were obtained using a high resolution transmission electron microscope (HRTEM) (JEOL-JEM 200CX). Selected area electron diffraction (SAED) studies were carried out on the as-quenched and heat treated samples.

The densities of the as-quenched glasses and that of the heat-treated ones were determined using Archimedes' principle with xylene as immersion liquid with an accuracy of $\pm$0.01. Using these values the volume fractions of the dispersed phase (SBT) in the glass matrix was computed. Rectangular plates (area $\approx$ 100 mm^2 and thickness $\approx$ 1 mm) of glasses and glass nanocomposites were polished prior to the electrical property studies. The major faces of the polished samples were gold sputtered and silver epoxy was employed to bond the leads. The capacitance (C_p) and the dielectric loss (D) measurements were carried out using an impedance gain phase analyser (HP 4194 A) in the frequency range 100 Hz–40 MHz at different temperatures (300–873 K). The temperature of the sample was controlled to an accuracy of $\pm$0.5 K and it was monitored using a Chromel–Alumel thermocouple placed very close to the sample. A two terminal capacitor configuration was employed for the present measurements. The real (ε_r') and the imaginary (ε_r'') parts of the dielectric constant were evaluated using the following relations.

$$\varepsilon_r' = \frac{C_p d}{A\varepsilon_0} \tag{1}$$

where d is the thickness and A the area of the electrode sample and ε_o is the permittivity of free space.

$$\varepsilon_r'' = \varepsilon_r' \tan\delta \tag{2}$$

The measured data (ε_r' and ε_r'') are transformed to Z' and Z'' (real and imaginary parts of the impedance) using the following standard relations:[11]

$$Z^* = \frac{1}{j\omega C_0 \varepsilon^*} \tag{3}$$

$$Z' = \frac{\varepsilon''}{\omega C_0(\varepsilon'^2 + \varepsilon''^2)} \tag{4}$$

$$Z'' = \frac{\varepsilon'}{\omega C_0(\varepsilon'^2 + \varepsilon''^2)} \tag{5}$$

where ω is the angular frequency, $2\pi f$. C_0 is the vacuum capacitance ($\varepsilon_0 A/d$). The results are presented in the complex impedance plane in which Z'' *versus* Z' are plotted on a linear scale. The value of the bulk resistance (R_b) is found by the low frequency intercept of the semicircle on the real axis (x-axis). The semicircle passes through a maximum at a frequency f_0 (relaxation frequency) and satisfies the condition

$$2\pi f_0 R_b C_b = 1 \tag{6}$$

From the above equation the value of bulk capacitance (C_b) is evaluated.

Glasses and glass nanocomposites for pyroelectric measurements were poled at 550 K by applying a high dc electric field for a few hours. Temperature dependencies of the pyroelectric coefficient, P, were measured by the direct Byer–Roundy technique,[12] over the temperature range 300 to 870 K. The pyroelectric coefficient was calculated using the relation

$$P(T) = \frac{(i/A)}{(dT/dt)} \tag{7}$$

where i is the pyroelectric current produced when the sample is subjected to heating, A is the electrode area of the sample and dT/dt is the heating rate. The heating rate used in the present experiment was 3 K min^{-1}. The room temperature value of P was obtained from the average value of 300–310 K. The P *vs.* E ferroelectric hysteresis loop was recorded at a switching frequency 50 Hz with a modified Sawyer–Tower circuit.[13] The values of remnant polarization (P_r) and the coercive field (E_c) were determined from the hysteresis loop.

The as-quenched and the heat-treated samples were polished to optical quality and the optical transmission and absorption spectra of these samples were recorded using a spectrophotometer (Hitachi U3000) in the wavelength range 190 nm to 900 nm. The absorption coefficient (α), related to the light that is transmitted out of a sample of thickness d, is given by

$$I = I_0 \exp(\alpha d) \tag{8}$$

where I_0 is the input intensity of the light that is incident on the sample. The absorption coefficient is represented as the Tauc equation:[14]

$$\alpha(v) = C\left[\frac{(hv - E_g)^2}{hv}\right] \tag{9}$$

where C is a constant, hv is the photon energy and E_g is the optical band gap energy. The value of the optical band gap energy was obtained from the above relation by extrapolating the absorption coefficient to zero absorption in the $(\alpha hv)^{1/2}$ *versus* hv plot.

The band tail associated with the valence band and conduction band, which are developed due to the potential fluctuations in the material, extend into the band gap and normally show an exponential behavior. The band tails are characterized by the band tail parameter ΔE (Urbach energy)[15] and given by

$$\alpha(v) \propto \exp\left(\frac{hv}{\Delta E}\right) \tag{10}$$

where ΔE was found as the inverse slope of the ln α *versus* hv plot.

The second harmonic (SH) intensity (532 nm) of the glass-ceramics of different compositions was measured at room temperature using the fundamental wave of a pulsed Nd : YAG laser *via* the Maker fringe method.[16]

3. Results and discussion

3.1. Differential thermal analyses

Fig. 1 (a–d) shows the DTA profiles of the representative compositions of the as-quenched samples. The shapes of all the

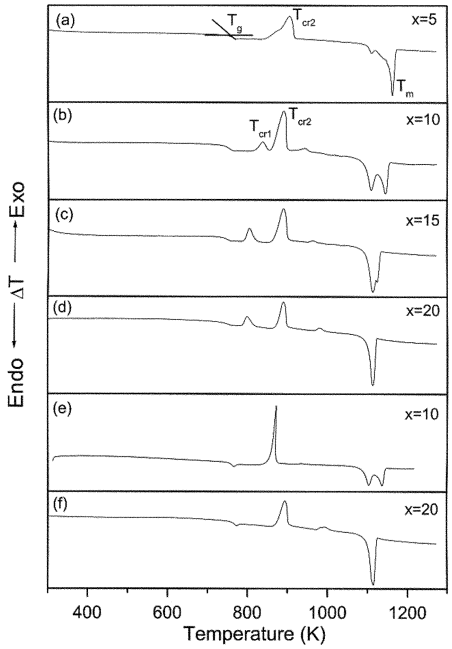

Fig. 1 Differential thermograms of the as-quenched (a–d) and heat-treated (e and f) (720 K/6 h) samples of various compositions.

curves are similar and confirm the glassy nature of all the as-quenched samples. These plots show endotherms, attributed to the glass transition temperature (T_g) in the temperature range 730–750 K, depending on the extent of x. The exotherms in the range 790–880 K correspond to the crystallization temperatures (T_{cr1} and T_{cr2}). The endotherms that are encountered around 1100 K are due to the melting of the glass composite. A well separated first exotherm (T_{cr1}) was observed only for those samples with $x \geqslant 10$. However, for $x = 5$ (Fig. 1a) we see distorted broad exothermic peaks, which could be split into two. For $x > 22.5$, the glass formation was difficult and the dispersed phase was precipitated out. Therefore, the compositions were restricted up to $x = 22.5$. As-quenched samples heat-treated isothermally at 720 K/6 h (near the onset of first exothermic peak, T_{cr1}) were subjected to DTA studies. It was noticed that the first exotherm (T_{cr1}) in the profile was absent and the rest of the features remained unaltered. Fig. 1 (e and f) shows the DTA patterns for the 720 K/6 h heat-treated sample for two representative compositions. The details of the phase crystallized near T_{cr1} are discussed latter in the XRD studies. The occurrence of the clear glass transition and crystallization of the host matrix of the heat-treated samples confirm that the host matrix is still in the glassy state, though it is embedded with nanocrystalline dispersoids of SBT.

Table 1 summarizes different thermal parameters *viz*. glass transition temperature (T_g), crystallization temperatures (T_{cr1} and T_{cr2}), melting temperature (T_m), thermal stability (ΔT, $T_{cr2} - T_g$) and glass formation parameter (K_{gl}) for both the as-quenched and heat-treated (720 K/6 h) samples. The T_{cr1} shifts towards lower temperatures as the molar percentage of SBT (x) increases in the LBO glass matrix. The crystallization temperature of the host glass matrix, T_{cr2}, for both as-quenched glass and heat-treated samples shifts towards higher temperatures as the SBT content (x) increases, suggesting that the thermal stability of the glass against crystallization (ΔT) increases with increase in x.

These thermal data were used to determine the glass formation parameter (K_{gl}), originally deduced by Hruby,[17] which is given by

$$K_{gl} = \frac{T_{cr} - T_g}{T_m - T_{cr}} \tag{11}$$

T_{cr} in the above equation refers to the crystallization temperature of the host glass matrix (T_{cr2}) in the present case. For glasses quenched under the same conditions, the onset of crystallization would be strongly dependent on the heating rate used in the DTA studies. In the present investigations the heating rate was kept constant (15 K min^{-1}) for all the compositions under study as K_{gl} do depend on the heating rate. K_{gl} is an indicator of the glass formation tendency for a wide variety of materials and it was proved that for good glass forming systems the value of $K_{gl} \geqslant 0.1$.[18] As listed in Table 1, K_{gl} increases with increase in x for both the as-quenched glass and heat-treated samples. The increase in K_{gl} is rapid in the as-quenched glass till $x = 12.5$ and subsequently it is gradual. On the other hand K_{gl} of the heat-treated sample is not that rapid. The K_{gl} of the as-quenched glass at any value of x is always higher than that of the heat-treated sample. This may be due to the presence of nanocrystalline SBT in the LBO glass structure, which modifies the network structure of the glass.

3.2. Structural studies

The XRD patterns recorded for all the compositions of the as-quenched sample ($0 \leqslant x \leqslant 22.5$) were confirmed to be amorphous. Fig. 2 (a) presents the XRD pattern for the

Table 1 Different thermal parameters and densities for the as-quenched and heat-treated (720 K/6 h) samples of various compositions.

Composition x	T_g/K	T_{cr1}/K	T_{cr2}/K	T_m/K	ΔT/K	K_{gl}	ρ/g cm^{-3}
As-quenched							
5	747		845	1097	98	0.39	2.726
7.5	746		853	1096	107	0.44	2.945
10	739	819	861	1093	122	0.53	3.022
12.5	729	800	866	1096	137	0.59	3.245
15	733	797	870	1098	137	0.60	3.568
17.5	735	794	875	1101	140	0.62	3.755
20	736	789	877	1102	141	0.63	4.047
22.5	737	788	883	1103	146	0.66	4.228
Heat-treated at 720 K/6 h							
5	744		837	1127	93	0.32	2.821
7.5	746		854	1120	108	0.40	3.101
10	754		858	1117	104	0.41	3.263
12.5	754		859	1106	105	0.43	3.44
15	754		867	1096	113	0.49	3.663
17.5	755		870	1097	115	0.51	4.057
20	757		874	1100	117	0.52	4.300
22.5	759		881	1101	122	0.56	4.423

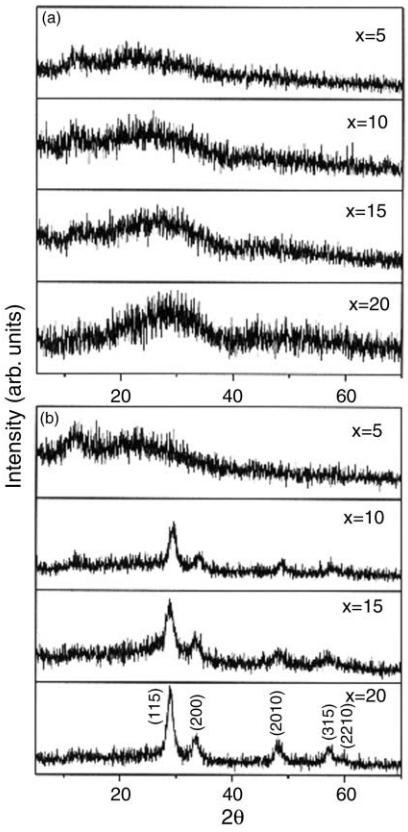

Fig. 2 XRD patterns for (a) the as-quenched and (b) the sample heat-treated at 720 K/6 h for the representative composition.

representative compositions of the as-quenched sample. These samples were colorless in the as-quenched form and turned yellowish when heat-treated at 720 K/6 h (just before the onset of the first exothermic peak in DTA). The XRD patterns of the samples of different compositions heat-treated isothermally at 720 K/6 h are shown in Fig. 2 (b). The clear crystalline peaks in these XRD patterns suggest that there is a selective crystallization at this stage of heat-treatment. The Bragg peaks were indexed to the diffraction lines (115), (200), (2010), (315) and (2210) of the monophasic crystalline SBT phase. It is interesting to note that only those compositions corresponding to $x \geqslant 10$ showed crystalline peaks in the XRD patterns. It was also observed that, at this stage of heat-treatment, no traces of crystalline LBO peaks were present in any of the compositions under study. The as-quenched samples of compositions $10 < x \leqslant 22.5$, heat-treated at 770 K/6 h (near the onset of crystallization, T_{cr1}) were transparent (deep yellowish) and the XRD depicted the presence of only monophasic crystalline SBT (not shown in the figure). On the other hand the heat-treated (770 K/6 h) samples for $x \leqslant 10$ were translucent and XRD showed the presence of LBO crystalline peaks in addition to that of SBT. It suggests that higher (>10 mol%) concentrations of SBT prevent the devitrification of LBO. It was also confirmed based on XRD studies that the LBO crystallization is confined only to the surface of the sample while that of SBT was found to be a bulk process. The XRD patterns obtained for unpolished flat plates of the samples ($x \leqslant 10$) heat-treated at 770 K/6 h showed peaks corresponding to an LBO crystalline phase along with that of SBT. The same samples when subjected to XRD studies subsequent to the removal of a few surface layers (to the extent of a few micrometres) did not reveal the presence of LBO peaks. The XRD patterns before and after removing the surface layers for the sample heat-treated at 770 K/6 h corresponding to the composition $x = 10$ are depicted in Fig. 3. Apart from the additional LBO crystallization for the samples heat-treated at

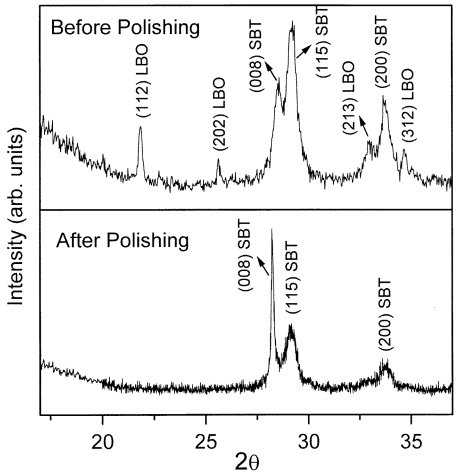

Fig. 3 XRD patterns for 770 K/6 h heat-treated sample ($x = 10$), before and after removing a few surface layers.

770 K, the intensities of the SBT peaks were also more than those of the samples heat-treated at 720 K. The full width at half maximum (FWHM) of the SBT peak for the 770 K heat-treated sample is less than that of the 720 K heat-treated sample. The SBT crystallite size in LBO matrix for the glass nanocomposite (770 K heat-treated) corresponding to the composition $x = 20$ from FWHM of the SBT peaks using Scherrer's equation was calculated to be 40 (± 5) nm. It was also noticed, based on the XRD studies that as the content of SBT in LBO increases, the FWHM decreases confirming an increase in crystallite size of SBT in LBO matrix.

The as-quenched glass and glass nanocomposites of different compositions under study were subjected to transmission electron microscopic studies to investigate into the amorphous/crystalline nature of the samples. In Fig. 4 (a), we show the transmission electron micrograph (TEM) along with selected area electron diffraction (SAED) patterns of the as-quenched glass for the representative composition corresponding to $x = 10$. This pattern clearly demonstrates the amorphous nature of the as-quenched glass and the micrograph shows sub-nano

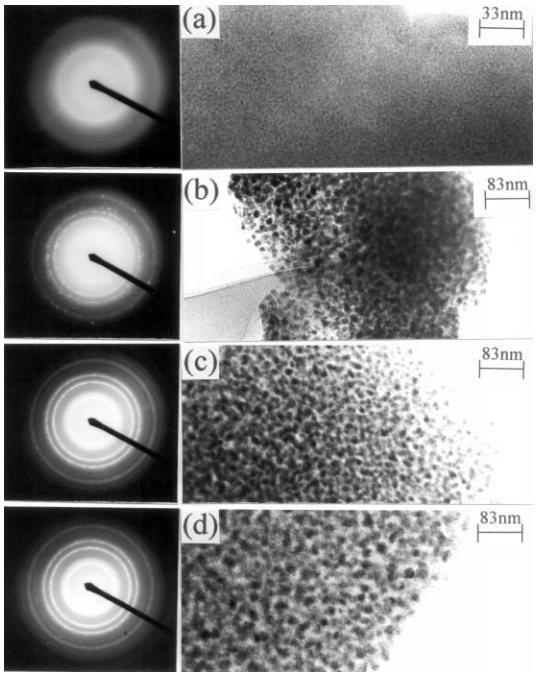

Fig. 4 TEM and SAED patterns of (a) as-quenched sample with $x = 10$ and heat-treated (720 K/6 h) samples corresponding to the compositions (b) $x = 10$, (c) $x = 15$ and (d) $x = 17.5$.

inclusions in the glassy matrix. Fig. 4 (b, c and d) shows the TEM and corresponding electron diffraction patterns of the heat-treated (720 K/6 h) samples for $x = 10$, 15 and 17.5 respectively. It is evident from the electron diffraction patterns that the crystallinity increases with increasing SBT content in LBO matrix. The *d*-values calculated from the electron diffraction patterns agree well with the literature values for SBT. The dark and nearly spherical phase in the TEM image is identified with the SBT crystallites, which is dispersed uniformly in the glass matrix of LBO. The average crystallite size of SBT phase increases gradually with increasing x. The average size of SBT crystallites for the compositions $x = 10$, 15 and 17.5 are 11, 14 and 19 nm respectively.

The influence of heat-treatment on these samples was also studied *via* TEM. Fig. 5 (a–c) shows the transmission electron micrographs along with SAED patterns (shown as insets) for the as-quenched glass, sample heat-treated at 720 K/6 h and 770 K/6 h respectively for $x = 20$. The electron diffraction patterns confirm their respective amorphous/crystalline states. It is clear from the micrographs that as the heat-treatment temperature increases from 720 K to 770 K, there is an increase

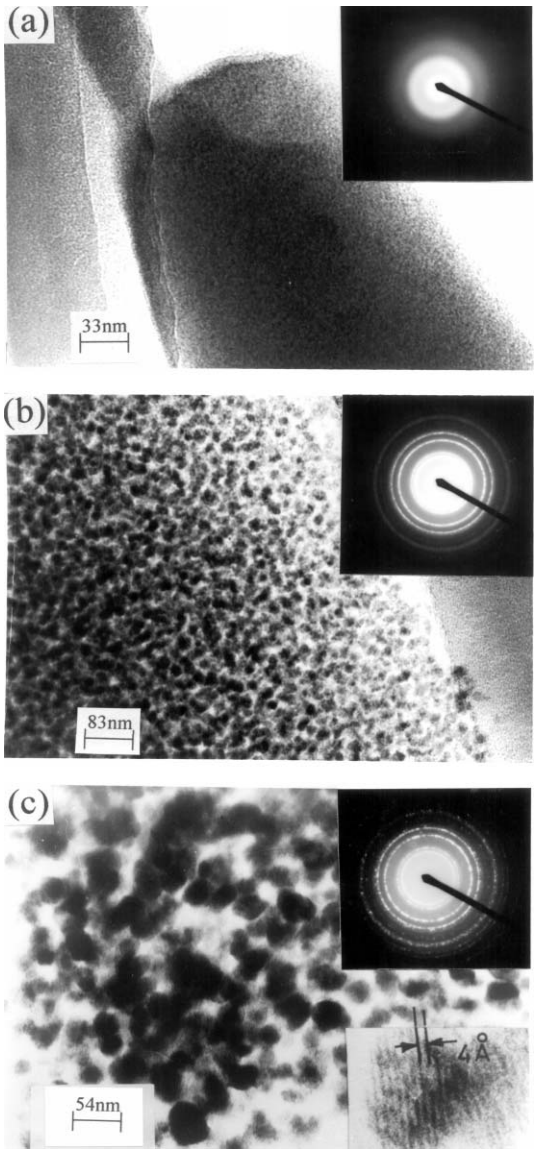

Fig. 5 Transmission electron micrographs of (a) the as-quenched sample (b) the sample heat-treated at 720 K/6 h and (c) the sample heat-treated at 770 K/6 h, with corresponding electron diffraction patterns (as insets) for the composition corresponding to $x = 20$. Inset (bottom) of (c) represents the high resolution lattice image of heat-treated (770 K/6 h) sample ($x = 20$).

(24 to 30 (± 5) nm) in crystallite size of SBT. A high resolution lattice image obtained for a crystallite of the sample heat-treated at 770 K/6 h is shown as inset (bottom) in Fig. 5 (c). The fringe spacing , which is about 4 Å, corresponds to one sixth of the *c*-parameter (006) of SBT and thus confirms the existence of a crystalline SBT phase in the LBO glass matrix.

The density measurements carried out at room temperature for the as-quenched and heat-treated samples for different values of x are listed in Table 1. The densities of all the present glass and glass nanocomposites lie in between those of lithium borate glass (2.284 g cm^{-3}) and strontium bismuth tantalate ceramics (8.04 g cm^{-3}). A gradual increase in the value of densities was observed, with increasing content of SBT in the LBO glass matrix. For any particular value of x, the heat-treated sample had a higher density than that of the as-quenched sample. The volume fraction of SBT present in the lithium borate glass matrix was calculated using the known densities of SBT and LBO and the measured densities of the glasses and glass nanocomposites.

3.3. Dielectric studies

The frequency response of ε_r' and D for the as-quenched glasses of representative compositions with $x = 5$, 10, 15 and 20 are shown in Fig. 6 (a and b). The low frequency dielectric dispersion is observed both in ε_r' and D. The frequency dispersion is strong for the glasses containing less SBT. The trend in the variation of ε_r' and D of the glasses heat-treated at 720 K/6 h (glass nanocomposites) , with frequency is similar to that of the as-quenched glasses (not shown in the figure). Fig. 7 depicts the variation of ε_r' and D, as a function of x (at 100 kHz) for the as-quenched and heat-treated samples. The relative permittivity increases and the dielectric loss decreases when the amount of SBT content in LBO increases for both the as-quenched and heat-treated samples. It was also noticed that ε_r' is higher, while the D value is lower, for the heat-treated samples than those of the as-quenched glass at any particular value of x. It is interesting to note that the dielectric loss of the glass nanocomposites is less by one order of magnitude than that of both the parent lithium borate glass and polycrystalline strontium bismuth tantalate ceramic. The D value of the glass nanocomposite corresponding to the composition $x = 20$ is 0.035 (at 100 kHz), whereas the values of D for lithium borate glass and polycrystalline strontium bismuth tantalate reported in the literature are 0.2 and 0.22 (at 100 kHz).[19,20] This is an important feature of these nanocomposites to be considered for pyroelectric detector applications.

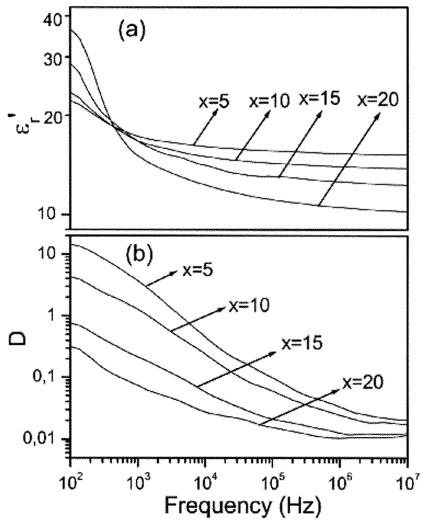

Fig. 6 Frequency response of (a) relative permittivity (ε_r') and (b) dielectric loss (D) for the as-quenched glass at 300 K for the representative compositions.

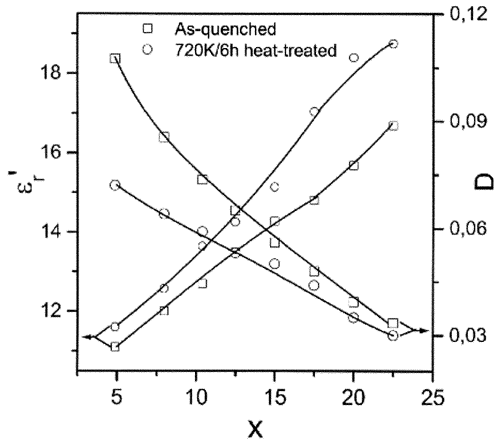

Fig. 7 Variation of relative permittivity (ε_r') and dielectric loss (D) for the as-quenched samples and samples heat-treated at 720 K for 6 h, with SBT content.

The dielectric behavior of the glass nanocomposites of the present kind could be explained using the model which was originally proposed by Stevels and Taylor[21,22] to understand the dielectric relaxation and ionic conductivity behavior of alkali silicate glasses. A crystalline material with long range order is considered to have regularly spaced and uniform height free energy barriers that are likely to impede the ionic jump. The vitreous solid, which is disordered at the molecular level, is expected to have a variation in the free energy barriers from site to site. In the present case (glass nanocomposites) in which all the sites are not equivalent, ions under dc or low frequency conditions can jump readily out of sites associated with low free energy barriers in the applied field direction but tend to pile up at sites with high free energy barriers resulting in the net polarization of the medium and as a consequence one would expect an increase in ε_r' at low frequencies. However, the increase in ε_r' with increasing x is attributed to the increase in interfacial polarization and connectivity, while the decrease in D (which is a significant result), in other words the ac conductivity, with increase in x is attributable to the impediment caused to the motion of Li^+ ions (which is understood to be the origin for the ac conduction mechanism in LBO glasses) by the distribution of spherical crystallites of SBT in the LBO glass matrix.

The variation of relative permittivity as a function of temperature at different frequencies for the as-quenched glass and glass nanocomposite (heat-treated at 720 K/6 h) for the composition corresponding to $x = 20$ is shown in Fig. 8 (a and b). The relaxation peak in the 370–600 K temperature range is attributed to the lithium ion hopping in the case of pure lithium borate single crystal and glass.[23,19] This peak shifts towards the higher temperature as the frequency is increased. The increase in ε_r' of the as-quenched sample with temperature is steep beyond 700 K and shows a small peak around 750 K due to the *in situ* crystallization of the SBT in the LBO glass matrix. This peak is absent in the ε_r' of the glass nanocomposite [Fig. 8 (b)] for which SBT is already in the crystalline form. However, the rapid increase in ε_r', with temperature in glass nanocomposite may be due to the rapid growth of SBT crystallites. Both as-quenched glass and glass nanocomposite show anomalies in ε_r' in the vicinity of the crystallization temperature of the host glass matrix. This peak temperature is comparable with that of the T_{cr} of LBO glass matrix encountered in DTA studies. It was also noticed that the temperature at which the peak in ε_r' occurs, shifts towards higher temperatures as the frequency increases. This is similar to the trend observed in the case of relaxor ferroelectrics[24] near the ferro–paraelectric transition. However, the dielectric data beyond 750K in the both the plots

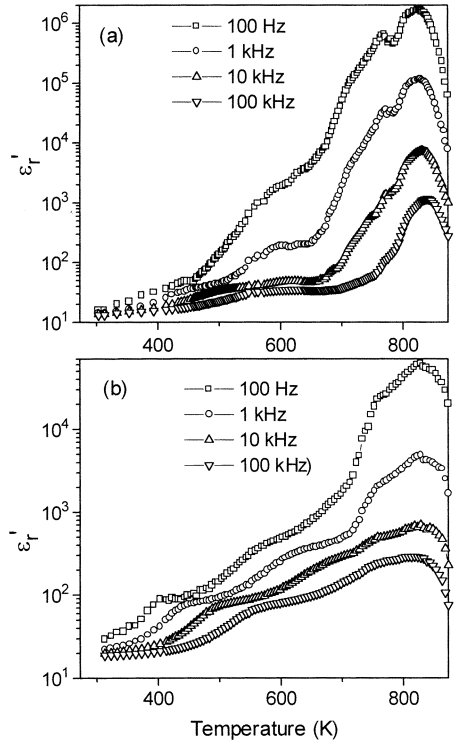

Fig. 8 Variation of ε_r' with temperature for (a) the as-quenched sample and (b) the sample heat-treated at 720 K/6 h for the composition corresponding to $x = 20$.

need to be corrected for a possible subtle change in the dimensions of the samples owing to the softening.

The dielectric loss, D, measured as a function of frequency at various temperatures for the glass nanocomposite corresponding to the composition $x = 20$ is depicted in Fig. 9. The frequency of the peaks (f_m) shifts towards higher values as the temperature of the measurement increases. The plot of ln f_m *versus* $1/T$ is linear within the observed temperature and frequency ranges (shown as inset in Fig. 9). Therefore f_m could represented by a simple Arrhenius formula

$$f_m = f_{m0} \exp\left[\frac{-W}{kT}\right] \tag{12}$$

where W is the activation energy for the thermally activated process and is found to be 0.78 eV.

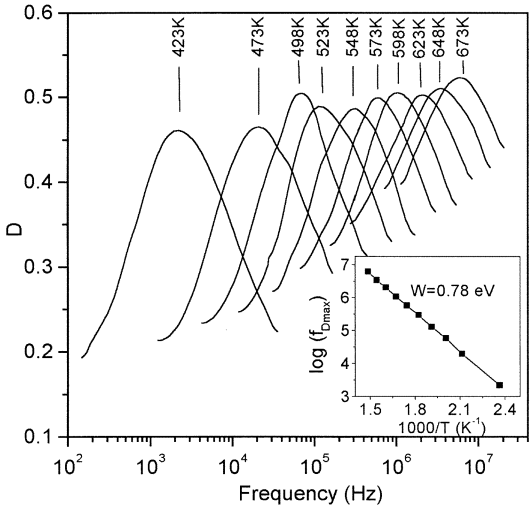

Fig. 9 Frequency response of dielectric loss (D) at various temperatures for the glass nanocomposite with $x = 20$. The inset shows the Arrhenius plot of ln $f_{D_{max}}$ *vs.* 1000/T.

3.4. Dielectric models

The physical properties of nanocomposites depend much upon the dispersion phase topology and volume fractions of the constituents. The practice of calculating the effective relative permittivity of an inhomogeneous composite material from the known values of the pure constituent phases, using different dielectric models, is common in the field of composite science. The effective relative permittivity (ε_{eff}) of the present glass nanocomposite was calculated using different dielectric models and it was found that the ε_{eff} calculated using Maxwell model coincides well with the experimentally found relative permittivity. The relative permittivity of the dispersed phase (SBT ceramic) being ε_1 and the host matrix (LBO glass) ε_2, the corresponding volume fractions are V_1 and V_2, respectively.

The effective relative permittivity of a diphasic composite comprising spherical crystallites with high relative permittivity dispersed in a matrix of low relative permittivity could very well be described by Maxwell's model.[25] According to this model the effective relative permittivity of the composite is given by

$$\varepsilon_{eff} = \frac{V_2\varepsilon_2\left(\frac{2}{3} + \frac{\varepsilon_1}{3\varepsilon_2}\right) + V_1\varepsilon_1}{V_2\left(\frac{2}{3} + \frac{\varepsilon_1}{3\varepsilon_2}\right) + V_1} \quad (13)$$

ε_{eff} calculated using this model (17.15 for $x = 20$) is in good agreement with the experimentally observed (17.05 for $x = 20$) relative permittivity of the glass nanocomposite. This could be well understood by invoking the transmission electron microscopic results. Transmission electron microscopy done on the glass nanocomposite revealed the presence of nearly spherical crystallites of SBT, more or less uniformly distributed in a continuous host glass matrix of LBO (Fig. 4) and thus satisfying one of the requirements based on which this model has been built. Therefore, it is inferred that the close agreement between the predicted and experimentally determined values may be attributed chiefly to the microstructural features that are associated with the glass nanocomposite.

3.5. Impedance analysis

It is known in the literature[26,27] that the dielectric relaxation does depend on the heterogeneity of the samples. Since the materials that are being dealt with in the present investigations are diphasic and heterogeneous in nature, we thought it worth adopting an impedance analysis approach, which is an ideal and powerful tool to probe into details such as bulk and grain boundary effects in ceramics. In the complex impedance plane plots (Cole–Cole) a single semicircle suggests the bulk and a second semicircle suggests the grain boundary effects. Each of the semicircles is represented by a single *RC* combination. A depressed semicircle, whose center lies below the real axis suggests a departure from the ideal Debye-like behavior. The inverse peak frequency of the semicircle indicates the relaxation time.

Complex impedance plots of the as-quenched and heat-treated (720 K/6 h) samples of the composition corresponding to $x = 20$, at various temperatures, are shown in Fig. 10 and 11. The impedance characteristics of both as-quenched and heat-treated samples are similar. However, one can notice an appreciable increase in impedance of the heat-treated sample at all frequencies and temperature when compared with as-quenched samples. For both the samples, at all temperatures we get a depressed semicircle with the center lying below the real axis, which is indicative of a non-Debye type of relaxation. Even though there are signs of a second semicircle appearing on the low frequency side , it was not complete due to the frequency limitation that is associated with our experimental facility. The appearance of second semicircle may be attributed to the presence of an amorphous matrix, which acts like a grain boundary between the crystallites. The presence of a single semicircle in the frequency range covered (100 Hz–40 MHz) in the present studies refers to the ac response of the crystallites embedded in the glass matrix. This may be interpreted in terms of the bulk response of the sample and a single parallel *RC* element. The bulk resistance of the sample (*i.e.* SBT crystallites embedded in an LBO glass matrix) is calculated by the intercept of the semicircle with the real axis on the lower frequency side.

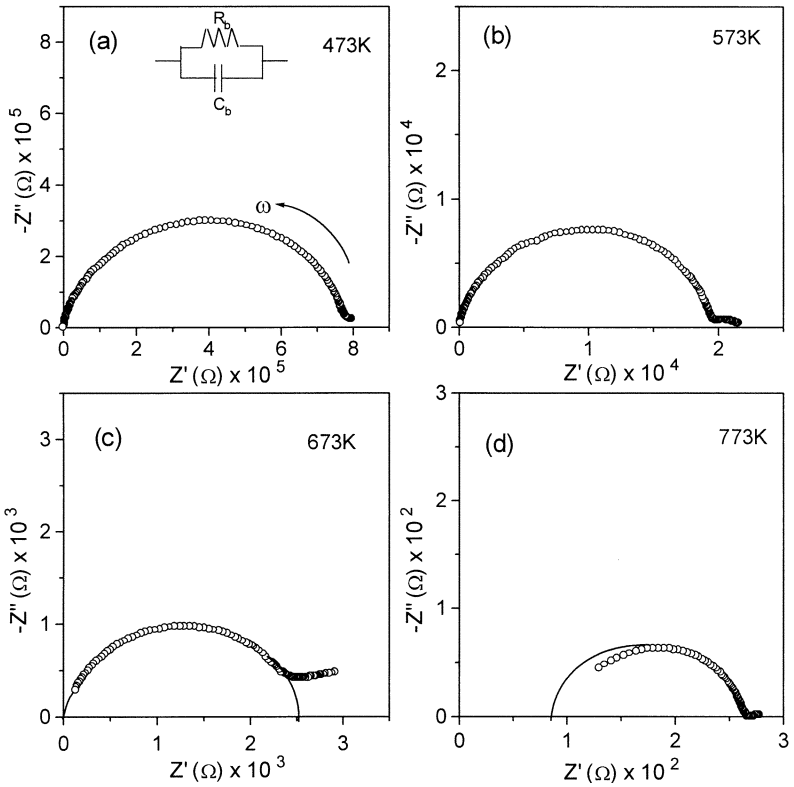

Fig. 10 Complex impedance plot at different temperatures for the as-quenched sample ($x = 20$), with the corresponding equivalent circuit.

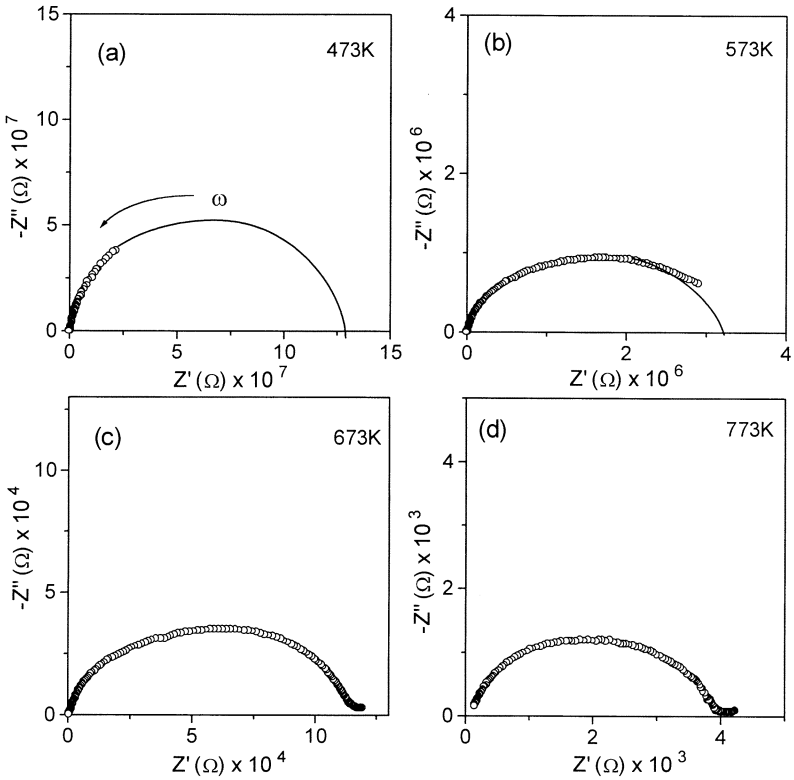

Fig. 11 Complex impedance plot at different temperatures for the sample heat-treated at 720 K/6 h (glass nanocomposite) for the composition corresponding to $x = 20$.

The bulk resistance of both the samples decreases when the temperature of the measurement increases. The bulk resistance, capacitance and relaxation frequencies of both the samples noted from the complex impedance plots at various temperatures are listed in Table 2. It is evident from Table 2 that the bulk resistance of the heat-treated sample is always higher than that of the as-quenched sample at all the temperatures in the present study. This is chiefly attributed to the presence of coarse crystallites of SBT in the LBO matrix, which impede the Li^+ ionic motion. These findings are very useful in explaining the lower dielectric loss associated with the heat-treated samples (glass nanocomposites) than those of the as-quenched glass.

3.6. Pyroelectric studies

The variation of pyroelectric coefficient, P, with temperature for the as-quenched and heat-treated (720 K/6 h) samples ($x = 20$) is shown in Fig. 12. The observed pyroelectric coefficient for both the samples is positive at room temperature. The pyroelectric coefficient of the as-quenched glass (27 $\mu C\ m^{-2}\ K^{-1}$) noted at room temperature is less than that of the heat-treated sample (53 $\mu C\ m^{-2}\ K^{-1}$). The as-quenched glass exhibits two peaks in the pyroelectric coefficient in the 600–850 K temperature range, which are attributed to the crystallization of SBT and LBO. However, these peak positions are lower than those observed in DTA studies. The difference is attributed to the difference in the time scales that are associated with these experiments . The sample heat-treated at 720 K/6 h also exhibits these peaks in the same temperature range. However, the intensity of the first peak is very small due to the fact that the crystallization of SBT has already occurred prior to the measurement and only grain growth and secondary crystallization of the remnant SBT occur at this stage.

The total pyroelectric coefficient of both the samples is positive, indicating that the pyroelectricity observed in these glasses and glass nanocomposites is of secondary type. The secondary pyroelectricity originates from the contribution arising from thermal expansion, elastic stiffness apart from pyroelectric effects. Due to the *in situ* crystallization and grain

Table 2 Bulk resistance (R_b), relaxation frequency (f_0) and bulk capacitance (C_b) of the as-quenched and heat-treated (720 K/6 h) samples ($x = 20$) at various temperatures

T/K	R_b/Ω	f_0/Hz	C_b/F
As-quenched			
473	7.89×10^5	1.11×10^4	1.82×10^{-11}
573	1.95×10^4	4.98×10^5	1.63×10^{-11}
673	2.52×10^3	3.92×10^6	1.61×10^{-11}
773	2.64×10^2	1.84×10^7	3.27×10^{-11}
Heat-treated at 720 K/6 h			
473	1.29×10^8	—	—
573	3.22×10^6	5.71×10^2	8.66×10^{-11}
673	1.15×10^5	1.98×10^4	7.02×10^{-11}
773	3.96×10^3	1.15×10^6	3.49×10^{-11}

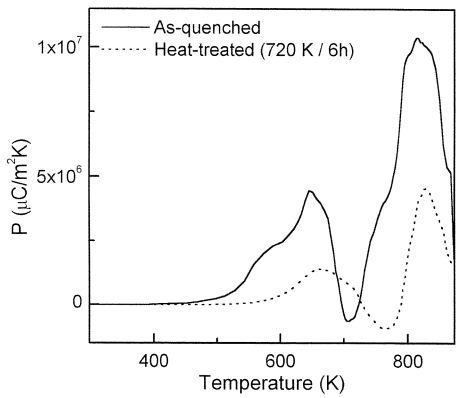

Fig. 12 Pyroelectric response of the as-quenched and heat-treated (720 K/6 h) samples, with temperature.

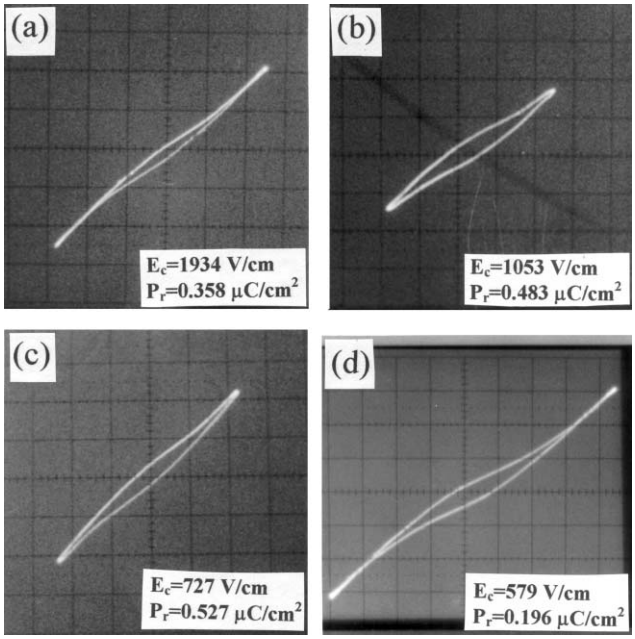

Fig. 13 The *P versus E* hysteresis loops for the glass nanocomposites recorded at 300 K for the compositions (a) $x = 5$, (b) $x = 15$ and (c) $x = 20$ and (d) the hysteresis loop for the glass nanocomposite recorded at 373 K with $x = 15$.

growth of the constituent phases near the exothermic peaks observed in DTA studies, the sample experiences a volume change and hence fluctuations in the thermal expansion characteristics. The contributions from thermal expansion are contemplated to be more to the observed total pyroelectric effect. Therefore, it is generalized that whenever there is a structural change occurring in the sample as a function of temperature variation, one would encounter anomalies in the pyroelectric coefficients. Since we have already nanometre sized crystallites in the heat-treated sample the peaks in the pyroelectric coefficient for the heat-treated sample are less strong.

3.7. Ferroelectric studies

The as-quenched samples (containing <1 nm crystallites of SBT) of different compositions of the present system did not exhibit well defined *P versus E* hysteresis loops. However, the samples heat-treated at 770 K/6 h (glass nanocomposite) showed the *P versus E* hysteresis loops at room temperature. The ferroelectric hysteresis loops recorded at room temperature for the glass nanocomposites of the composition corresponding to $x = 5$, 15 and 20 are shown in Fig. 13 (a), (b) and (c), respectively. These loops are reminiscent of the ferroelectric nature of the bismuth layered ferroelectric oxides. It is evident from Fig. 13 that the electric field required to switch the direction of spontaneous polarization (coercive field, E_c) decreases when the amount of SBT present in the LBO increases.

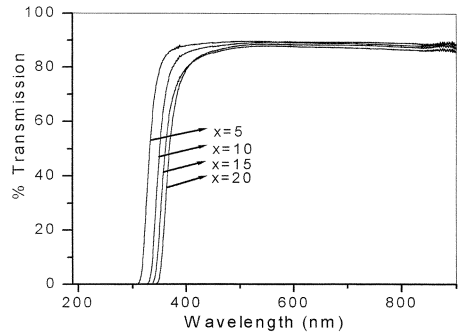

Fig. 14 The optical transmission spectra (uncorrected for the reflection losses) for the polished as-quenched glasses.

For instance E_c for $x = 5$ composition is 1934 V cm^{-1} where as E_c for $x = 20$ is only 727 V cm^{-1}. The presence of higher amounts of SBT crystallites increases the remnant polarization (P_r) of the glass nanocomposite. When the composition varies from $x = 5$ to 20 (*i.e.* the crystallite size increases from 10–40 nm), the remnant polarization increases from 0.358 to 0.527 μC cm^{-2}. The presence of nanocrystals of SBT in an amorphous LBO matrix helped in establishing the ferroelectric behavior in these glass nanocomposites. However, the P_r values of the present glass nanocomposites are much less (which is attributed to the crystallite size) than that obtained for both bulk ceramics ($P_r = 4$μC cm^{-2}) and thin films of pure SBT (containing micrometre sized crystallites).[28] The ferroelectric studies were also carried out at higher temperatures; the loop recorded at 373 K for the composition corresponding to $x = 15$ is shown in Fig. 13 (d). It was noticed that the P_r and E_c values decrease with increase in temperature of measurement and the values are presented in Fig. 13 (d).

3.8. Linear and nonlinear optical properties

The optical transmission spectra for the as-quenched glasses of the representative compositions $x = 5$, 10, 15 and 20 are shown in Fig. 14. All these glasses have good transparency ($\sim$90%) in the 400–900 nm wavelength range. Below 400 nm, the percentage transmission becomes zero at a characteristic wavelength called λ_{cutoff} (lower wavelength cutoff). The λ_{cutoff} shifts towards the higher wavelength side (red shift) when the SBT content (x) increases for all the compositions under study and is shown in Table 3. Apart from the dependency on x, the λ_{cutoff} also depends upon the heat-treatment temperature. The effect of heat-treatment on the transmission characteristics of the sample corresponding to the composition $x = 20$ is shown in Fig. 15. In Fig. 15, we see a red shift when the heat-treatment temperature (*i.e.* the crystallite size of SBT) increases. λ_{cutoff} for the sample heat-treated at 720 K/6 h with various SBT content (x) is also listed in Table 3.

The optical bandgap energies (E_g) of both the as-quenched and heat-treated (720 K/6 h) samples derived from absorption spectra are shown in Table 3. It is observed that E_g of both the

Table 3 The lower wavelength transmission cut off (λ_{cutoff}), optical bandgap energy (E_g) and Urbach energy (ΔE) for the as-quenched and heat-treated (720 K/6 h) samples of various compositions

	As-quenched			Heat-treated (720 K/6 h)		
Composition x	λ_{cutoff}/nm	E_g/eV	ΔE/eV	λ_{cutoff}/nm	E_g/eV	ΔE/eV
5	308	3.75	0.135	311	3.62	0.148
7.5	316	3.71	0.128	358	3.21	0.125
10	325	3.63	0.124	365	3.07	0.135
12.5	330	3.59	0.121	376	2.94	0.120
15	335	3.53	0.122	384	2.89	0.119
17.5	339	3.43	0.128	389	2.82	0.124
20	342	3.35	0.129	393	2.78	0.123
22.5	344	3.33	0.136	397	2.69	0.192

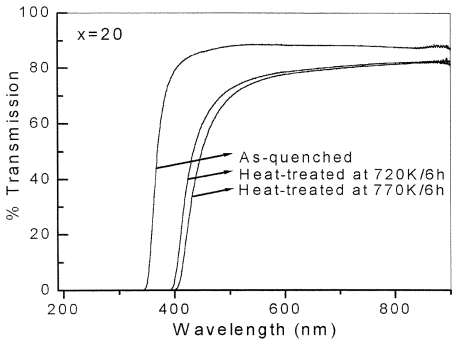

Fig. 15 The optical transmission spectra (uncorrected for the reflection losses) for the polished glass and glass nanocomposite (heat-treated at 720 K and 770 K for 6 h) samples corresponding to the composition $x = 20$.

samples decreases with increasing x, indicating that dispersion of more SBT produces energy levels that are closer. It was also noticed that the bandgap energy of heat-treated samples is lower than that of the as-quenched glasses. Urbach energy (width of band tails extended into the bandgap, ΔE) obtained from the slopes of the linear region in the ln $\alpha(v)$ against hv plot is used to characterize the degree of disorder in amorphous and crystalline systems. Materials with larger Urbach energy would have a greater tendency to convert weak bonds into defects. Consequently, the defect concentration could be decided by the measure of Urbach energy. The Urbach energy values for both as-quenched and heat-treated samples for various compositions are listed in Table 3. The lowest Urbach energy was observed for the compositions in the range $x = 12.5$ to 15 for both the as-quenched and heat-treated samples, suggesting the possibility of long range order locally arising from the minimum in the number of defects as compared to the other compositions.

The refractive indices of the polished glasses and glass nanocomposites were measured at room temperature using an ellipsometric technique at a wavelength of 6328 Å (He–Ne laser). The refractive index (n) increases appreciably with SBT content till $x = 15$; subsequently the increase in n is not that significant. It was observed that the presence of crystalline SBT (*i.e.* heat-treatment at 770 K/6 h) notably increases the refractive index of the sample. These values of refractive indices are shown in Table 4. The refractive index is dependent upon the composition of the material. The refractive index could be expressed in terms of density (ρ) and molecular weight (M) of the system by the well known Lorentz–Lorenz formula:[29–31]

$$R_m = \frac{(n^2-1)}{(n^2+2)}\left(\frac{M}{\rho}\right) \quad (14)$$

where R_m is the molar refraction, which is proportional to the mean polarizability (α_m) according to the relation

$$R_m = \frac{4\pi N\alpha_m}{3} \quad (15)$$

where N represents Avogadro's number or, more strictly, the number of polarizable ions per mole. The values of the molar refraction and mean polarizability of the as-quenched and heat-treated samples were evaluated using eqn. (14) and (15) and are given in Table 4. Both R_m and α_m monotonically increase with increasing SBT content for these samples. It should also be noted that the values of R_m and α_m are higher for the heat-treated sample than those of the as-quenched one. The mean polarizabilities of these glasses and glass nanocomposites are comparable, rather better than that of TeO_2 based glasses.[32] The compositional dependence of $\chi^{(3)}$ in La_2O_3–TeO_2 binary glasses was studied by Kim *et al.*[33] using the empirical approximation

$$\chi^{(3)} = C'(n^2+2)^3(n^2-1)\alpha_m \quad (16)$$

where C' is a constant. It has been shown that $\chi^{(3)}$ increases with increasing α_m and is proportional to the term $(n^2 + 2)^3(n^2 - 1)\alpha_m$. We have calculated this term from the known values of n and α_m for all the compositions and found that there was an increase in this value with increasing x. Therefore, it is expected that $\chi^{(3)}$ values of the present system would be higher for compositions containing higher SBT content. It is also inferred that $\chi^{(3)}$ values of heat-treated samples could be higher than those of the as-quenched one.

Fig. 16 depicts the variation of second harmonic (SH) intensity with angle of incidence of Nd : YAG laser light for the glass nanocomposites (heat-treated at 770 K/6 h) corresponding to the composition $x = 5$, 15 and 20. It is clear from Fig. 16 that the dependence of SH intensity on the angle of incidence is weak for the compositions with $x = 5$ and 15. However, there is an appreciable change in the SH intensity with the angle of incidence for the composition corresponding to $x = 20$. We believe that the higher value of SHG for $x = 20$ could be due to the presence of larger crystallites of SBT as compared to $x = 5$ and 15. The absolute values of the SH intensities are taken at the maximum positions for all the compositions, along with the SH intensity of the Z-cut quartz crystal to determine the d_{eff} of these samples. The d_{eff} of the glass nanocomposites corresponding to the compositions $x = 5$, 15 and 20 were computed to be 0.255, 0.264 and 0.373 pm V^{-1}, respectively with reference to quartz (d_{11} of quartz = 0.5 pm V^{-1}).

Table 4 Various optical parameters for the as-quenched and heat-treated (770 K/6 h) samples

Sample	x	n	R_m/cm^3 mol^{-1}	$\alpha_m \times 10^{-23}$/cm^3
As-quenched	5	1.542	24.39	0.967
	10	1.594	28.45	1.128
	15	1.644	29.98	1.189
	20	1.654	30.57	1.213
Heat-treated	15	1.722	31.93	1.266

Conclusions

Nanocrystallization was demonstrated *via* controlled crystallization of the $(100 - x)Li_2B_4O_7$–$xSrBi_2Ta_2O_9$ glassy system. XRD and electron diffraction studies with a limit of detection of 5% permit the conclusion that the crystallites are SBT embedded in an LBO matrix. An increase in crystallite size of SBT on the nanometre scale has been observed with increase in both the composition and the heat-treatment temperature. The relative permittivities of the glasses as well as glass nanocomposites increase with increase in SBT content, whereas the dielectric loss decreases. This feature along with that of an

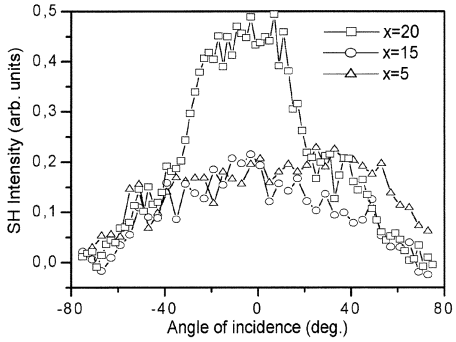

Fig. 16 SH intensities (532 nm) for the glass nanocomposites of three representative compositions as a function of the incident angle of laser (1064 nm).

increase in impedance has been very promising for considering the present composites for various technological applications. The ε_r' values predicted using Maxwell's model agree well with the experimentally determined values of the glass nanocomposites. The pyroelectric coefficient for the glass nanocomposite is significantly high. The most interesting aspect of the present investigations has been the observation of a ferroelectric hysteresis loop at 300 K in the glass nanocomposites. The optical transmission characteristics (*viz.* λ_{cutoff}, E_g) could be tailored depending on the amount of SBT present in the glass matrix. The Urbach energy derived from the absorption spectra for the glasses and glass nanocomposites suggested that the compositions in the range $x = 12.5$ to 15 show a minimum in the number of defects compared with those of the other compositions. The values of refractive index, polarizability and third order nonlinear optic susceptibility for the glass nanocomposites were larger than those of the as-quenched glasses. The observation of intense second harmonic generation in the glass nanocomposites is yet another significant result.

Acknowledgement

The authors thank the Council of Scientific and Industrial Research for the financial grant. Also their thanks are due to Professor T. Komatsu and Mr Y. Takahashi of Nagaoka University of Technology, Japan for their help in the measurement of SHG intensities and Dr G. N. Subbanna of Indian Institute of Science, Bangalore for TEM work.

References

1 K. Amanuma, T. Hase and Y. Miyasaka, *Appl. Phys. Lett.*, 1995, **66**, 221.
2 T. Mihara, H. Yoshimori, H. Watanabe and C. A. Paz de Araujo, *Jpn. J. Appl. Phys.*, 1995, **34**, 5233.
3 R. Dat, J. K. Lee, O. Auciello and A. I. Kingon, *Appl. Phys. Lett.*, 1995, **67**, 572.
4 T. C. Chen and S. B. Desu, *Phys. Status Solidi A*, 1998, **167**, 215.
5 W. F. Zhang, M. S. Zhang, Z. Yin, Y. Z. Gu, Z. L. Du and B. L. Yu, *Appl. Phys. Lett.*, 1999, **75**, 902.
6 Z. Huang, P. Yang, Y. Chang and J. Chu, *J. Appl. Phys.*, 1999, **86**, 1771.
7 G. Senthil Murugan and K. B. R. Varma, *J. Non-Cryst. Solids*, 2001, **279**, 1.
8 M. V. Shankar and K. B. R. Varma, *J. Non-Cryst. Solids*, 1999, **243**, 192.
9 G. Senthil Murugan, K. B. R. Varma, Y. Takahashi and T. Komatsu, *Appl. Phys. Lett*, 2001, **78**, 4019.
10 T. Sugawara, R. Komatsu and S. Uda, *Solid State Commun.*, 1998, **107**, 233.
11 J. R. Macdonald, *Impedance Spectroscopy*, Wiley, New York, 1987.
12 R. L. Byer and C. B. Roundy, *Ferroelectrics*, 1972, **3**, 333.
13 C. B. Sawyer and C. H. Tower, *Phys. Rev.*, 1930, **35**, 269.
14 J. Tauc, in *Optical properties of solids*, ed. F. Abeles, North-Holland, Amsterdam, 1969, p. 227.
15 F. Urbach, *Phys. Rev.*, 1953, **92**, 1324.
16 P. D. Maker, R. W. Terhune, M. Nisenoff and C. M. Savage, *Phys. Rev. Lett.*, 1962, **8**, 21.
17 A. Hruby, *Czech. J. Phys.*, 1972, **B22**, 1187.
18 D. D. Thornburg, *Mater. Res. Bull.*, 1974, **9**, 1481.
19 G. Senthil Murugan, G. N. Subbanna and K. B. R. Varma, *Ferrelectrics Lett.*, 1999, **26**, 1.
20 Jing Si Yang and Xiang Ming Chen, *Mater. Lett.*, 1996, **29**, 73.
21 J. M. Stevels, *Handbuch der physik*, ed. S. Flugge, Springer-Verlag, Berlin, 1957, **vol. 20**, p. 372.
22 (*a*) H. E. Taylor, *J. Soc. Glass Technol.*, 1957, **41**, 350T; (*b*) 1959, **43**, 124T.
23 S.-u. Furusawa, S. Tange, Y. Ishibashi and K. Miwa, *J. Phys. Soc. Jpn.*, 1990, **59**, 2532.
24 T. R. Shrout and A. Halliyal, *Am. Ceram. Soc. Bull.*, 1987, **66**, 704.
25 J. C. Maxwell, *A treatise on Electricity and Magnetism*, Dover Publishing Co., New York, 1954.
26 S. Lanfredi and A. C. M. Rodrigues, *J. Appl. Phys.*, 1999, **86**, 2215.
27 D. C. Sinclair and A. R. West, *Phys. Rev. B*, 1989, **39**, 13486.
28 K. Shoji, M. Aikawa, Y. Uehara and K. Sakata, *Jpn. J. Appl. Phys.*, 1998, **37**, 5273.
29 M. B. Volf, *Glass Science and Technology*, Elsevier, Amsterdam, 1984, **vol. 7**, p. 43.
30 H. A. Lorentz, *Wied. Ann.*, 1880, **9**, 641.
31 R. Lorenz, *Wied. Ann.*, 1880, **11**, 70.
32 Raouf El-Mallawany, *J. Appl. Phys.*, 1992, **72**, 1774.
33 S. H. Kim, T. Yoko and S. Sakka, *J. Am. Ceram. Soc.*, 1993, **76**, 865.